ChemComm

COMMUNICATION

View Article Online
View Journal | View Issue

Cite this: *Chem. Commun.*, 2018, **54**, 12654

Received 31st August 2018,
Accepted 18th October 2018

DOI: 10.1039/c8cc07098a

rsc.li/chemcomm

A charge-separated diamondoid metal–organic framework†

Sheela Thapa,[a] Eshani Hettiarachchi,[b] Diane A. Dickie,‡[a] Gayan Rubasinghege*[b] and Yang Qin*[a]

We report the synthesis, characterization, and gas adsorption analyses of a new charge-separated metal–organic framework (MOF), UNM-1 ($C_{52}H_{16}BCuF_{16}N_4$), possessing diamondoid structures, assembled from an anionic tetrahedral borate ligand and cationic Cu(I) metal ion. The resulting MOF structure displays four-fold interpenetration, resulting in high environmental stability, and at the same time possesses relatively large surface area (SA_{BET} = 621 m^2 g^{-1}) due to the absence of free ions. Gas adsorption measurements revealed temperature-dependent CO_2 adsorption/desorption hysteresis and large CO_2/N_2 ideal selectivities up to *ca.* 99 at 313 K and 1 bar, suggesting potential applications of this type of charge-separated MOFs in flue gas treatment and CO_2 sequestration.

Metal–organic frameworks (MOFs) have become an emerging field of intensive scientific research over the past few decades.[1] From limitless combinations of metal centers and organic ligands, a vast number of MOF materials have been developed and studied, leading to microporous scaffolds with precisely tunable surface areas, pore volumes, pore sizes and shapes, and surface functionalities.[2–4] The majority of the MOF structures studied to date contain charge-neutral metal clusters as nodes, or secondary building units (SBUs), connected by organic struts that are also non-charged, leading to an overall charge-neutral framework. In these structures, the positive charges on metal atoms are immediately balanced by surrounding anionic ligands, *e.g.*, carboxylates, and as a consequence, there are no exposed ionic species or accessible local electric fields within the MOF frameworks. On the other hand, a sub-class of MOFs known as ionic MOFs have emerged and attracted significant research attention.[5,6] These ionic MOFs contain isolated charged centers, either positive or negative, at the metal nodes or on the organic ligands. The local electric fields, electrostatic interactions, and/or coordinating effects generated by these isolated charges can exert stronger interactions with polar substrates and molecules with high polarizability, than simple van der Waals interactions typically found in non-ionic MOF materials.[7,8] Most of the ionic MOFs reported to date contain a single type of charge, either positive or negative, decorated covalently onto the framework, which leaves the free charge-balancing counter-ions within the pores. These counter-ions, depending on their sizes, unavoidably reduce accessible pore volumes of the MOF and can potentially occlude pore openings and inhibit adsorption of guest molecules. In this regard, it is appealing to incorporate both positive and negative charges at fixed distances and precisely controlled locations into one framework structure, forming the so-called charge-separated, or zwitterionic MOFs that can possess both the favorable interaction properties of ionic MOFs and free pore spaces as in non-ionic MOFs.

The existing examples of charge-separated MOFs are relatively scarce and mainly utilize zwitterionic organic ligands containing both cationic and anionic species, *e.g.*, ligands containing both carboxylate and pyridinium,[9–15] imidazolium,[16,17] or metallo-porphyrin moieties,[18] which upon complexation with cationic metal ions lead to charge-separated MOFs with or without the need for free charge-compensating counter-ions. Ziegler and coworkers have systematically explored the application of anionic tetrakis(imidazolyl)borate ligand in constructing charge-separated MOF structures through coordination with different metals.[19–22] When the metal ions possess oxidation state of +1 and coordination number of 4, three dimensional charge-separated MOFs are formed with an overall charge neutrality and the absence of free ions.[23] Although the four B–N bonds are arranged in tetrahedral geometry at the boron center in these borate ligands, due to the off-set angle between the B–N and N–metal bonds at *ca.* 145°,

[a] *Department of Chemistry & Chemical Biology, University of New Mexico, MSC03-2060, 1 UNM, Albuquerque, NM 87131, USA. E-mail: yangqin@unm.edu*
[b] *Department of Chemistry, New Mexico Institute of Mining and Technology, 801, Leroy Place, Socorro, NM 87801, USA. E-mail: gayan.rubasinghege@nmt.edu*

† Electronic supplementary information (ESI) available: Synthetic details, NMR spectra, single crystal data, TGA histogram, gas adsorption isotherms, IAST calculation and results, Q_{ST} calculation and results. CCDC 1865216. For ESI and crystallographic data in CIF or other electronic format see DOI: 10.1039/c8cc07098a

‡ Current address: Department of Chemistry, P. O. Box 400319, University of Virginia, Charlottesville, VA, 22904, USA.

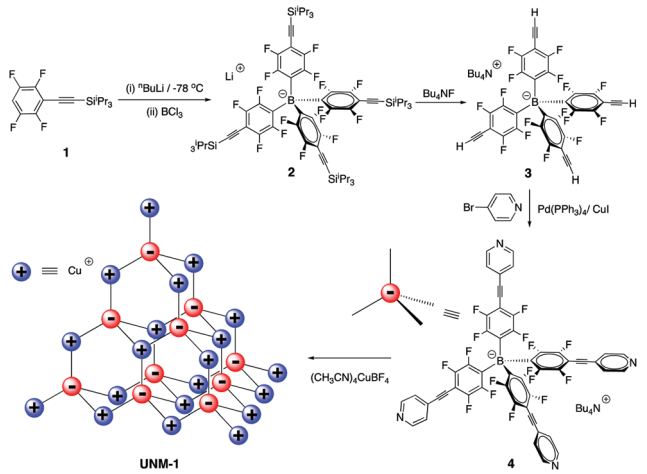

Scheme 1 Synthesis of ligands and schematic representation of the structure of **UNM-1**.

rotation around these single bonds can lead to a variety of conformations that make construction of ordered three dimensional structures difficult and hard to predict.[24] In this regard, borate ligands that possess colinear boron-organic-metal arms are preferred. In this report, we describe the synthesis of such a borate ligand containing tetrafluorophenylethynyl pyridine arms (**4**) and its coordination with Cu(I) ions for the formation of a charge-separated MOF, **UNM-1**. The synthesis of compounds **1–3** leading to ligand **4** was adapted from previously published procedures[25] and is summarized in Scheme 1. Sonogashira coupling of **3** with 4-bromopyridine led to the borate ligand **4** without the loss of tetrabutylammonium counter-ions. Compound **4** was fully characterized by multi-nuclear NMR spectroscopy (ESI†). Briefly, a single sharp ^{11}B NMR signal at −16.3 ppm and two ^{19}F signals at −129.9 and −139.7 ppm were observed, consistent with literature reported values for **3**.[25] The ^{13}C NMR signals were not reported in the original synthesis of **3**, so our signal assignments were based on an analogous compound, lithium tetrakis(4-bromotetrafluorophenyl)borate.[26] Two sets of doublets at 148.2 and 145.7 ppm having $^{1}J_{CF}$ coupling constants of 241 and 255 Hz are assigned to the F_4-phenyl carbon atoms *ortho*- and *meta*- to the boron center, respectively. The *ipso*-carbon appears as a broad signal ranging from 132 to 134 ppm caused by the splitting effects from ^{1}J boron and ^{2}J fluorine atoms. The F_4-phenyl carbon *para*- to boron center is a triplet at 98.9 ppm with a $^{2}J_{CF}$ coupling constant of 14 Hz. The two triple bond carbon signals appear at 96.0 and 80.5 ppm, while the signals from the pyridine rings are relatively enhanced and located at 149.9, 130.5 and 125.5 ppm, respectively. Integration of the ^{1}H NMR signal confirms that there is one tetrabutylammonium cation per borate anion.

UNM-1 was synthesized through an interfacial diffusion method, in which an CH_3CN solution of $(CH_3CN)_4CuBF_4$ was laid on top of a CH_2Cl_2 solution of borate **4**. Orange needle-shaped crystals of **UNM-1** were obtained after three days with *ca.* 74% yield based on **4**. The single crystal X-ray diffraction analysis is summarized in Fig. 1, Fig. S5 and Table S1 (ESI†).

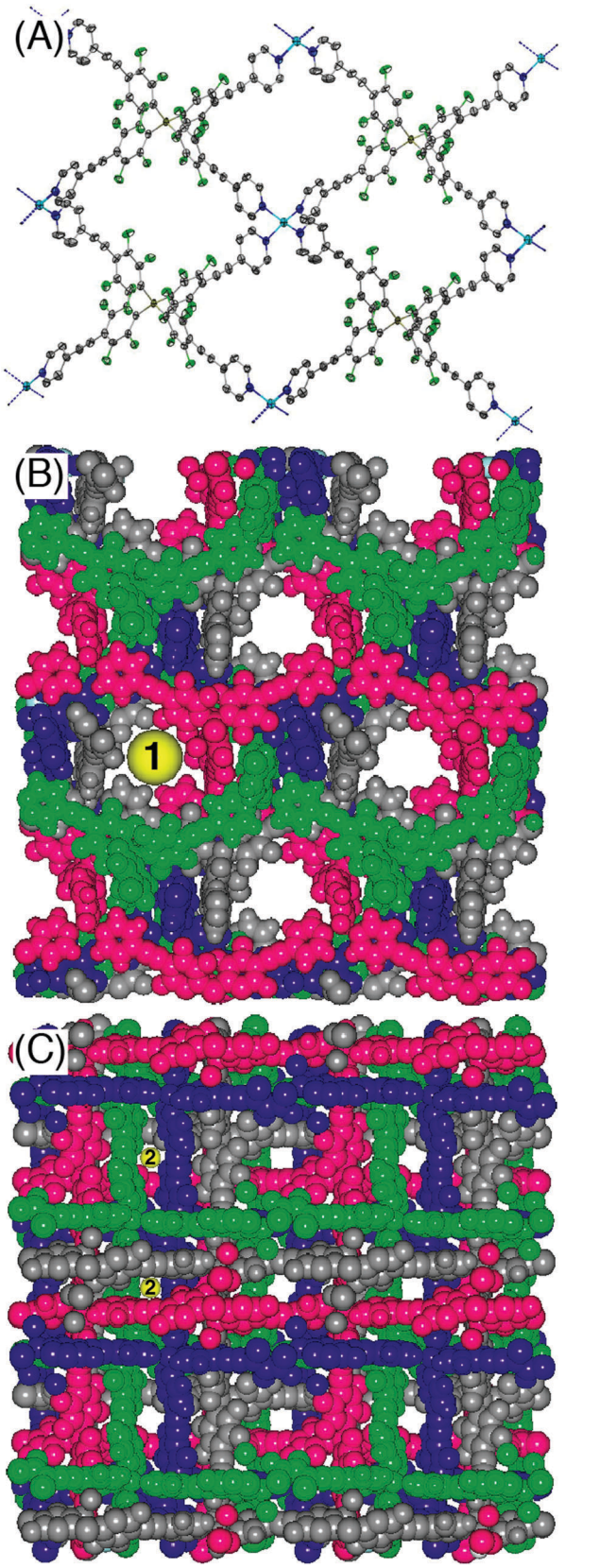

Fig. 1 (A) Single crystal X-ray structure of **UNM-1**. (B) Space-filling model of a 2 × 2 × 2 unit cell viewed from the *Y*-axis; and (C) space-filling model of a 2 × 2 × 2 unit cell viewed from the *Z*-axis.

UNM-1 crystalizes in the tetragonal crystal system with space group $I\bar{4}$ and unit cell dimension of $a = b = 23.5586(7)$ Å and $c = 24.6516(9)$ Å. The coordination environment around the boron and copper atoms is close to tetrahedral, with dihedral angles around boron centers ranging from 101° to 116° and those around copper centers from 100° to 121°, leading to an overall diamondoid-like net as shown in Fig. 1A and Fig. S5 (ESI†). One unique feature of the structure of **UNM-1** is the four-fold interpenetration as color-coded in Fig. 1(B and C), which is likely caused by the relatively long arms in borate ligand **4**, leading to a boron–copper separation distance of *ca.* 13.3 Å. From the space-filling model of a 2 × 2 × 2 unit cell viewed from the *X*- or *Y*-axis (Fig. 1B) and from the *Z*-axis (Fig. 1C), the crystal structure is porous with straight channels having two different pore sizes (yellow spheres labeled 1 and 2 for visual assistance). The larger channels are approximately circular in shape and *ca.* 7.4 Å in diameter. The smaller channels have alternating square and octahedral shapes, both of which possess pore size of *ca.* 2.7 Å.

UNM-1 is stable under ambient conditions as the powder X-ray diffraction (PXRD) pattern of **UNM-1** after drying under high vacuum at room temperature for 24 h and being stored in air for a week (Fig. S6, red trace, ESI†) closely matches that of the simulated pattern from single crystal X-ray data (Fig. S6, black trace, ESI†). The water stability of **UNM-1** was tested by soaking a few MOF crystals in water for 48 h and subjected to PXRD measurements after drying under high vacuum for 24 h. Again, no significant changes in diffraction pattern were observed (Fig. S6, ESI†). Changes in the XRD patterns of **UNM-1** could be observed after soaking the crystals in pH 4 and pH 10 aqueous solutions for 48 h, but the major scattering peaks remained, indicating certain stability of **UNM-1** under mildly acidic and basic conditions. The crystals disintegrated under pH 1 and pH 13 conditions, as shown by the complete disappearance of scattering signals in XRD profiles (Fig. S6, ESI†). Even after repeated gas adsorption trials with different gases at various temperatures (*vide infra*), the main features of PXRD pattern still remain, except becoming broader (Fig. S6, green trace, ESI†) indicating retention of the basic crystal structure but loss of long-range order. Furthermore, thermogravimetric (TGA) analysis of **UNM-1** (Fig. S7, ESI†) under N_2 shows *ca.* 2–3% weight loss up to 150 °C, likely due to loss of trapped solvent and water molecules, and no decomposition up to *ca.* 300 °C with a total 50% weight loss at 600 °C. We ascribe the observed stability of **UNM-1** to its four-fold interpenetration geometry that interlocks each layer and prevents dislocation.

The surface area of **UNM-1** was estimated by multi-point Brunauer–Emmett–Teller (BET) formalism through N_2 adsorption measurements at 77 K and the isotherm is shown in Fig. S8 (ESI†). The isotherm shows Type-I adsorption behaviour that confirms the microporous nature of **UNM-1**. Linear fit (Fig. S9, ESI†) between partial pressures (P/P_0) 0.05 and 0.30 gives the average BET surface area (SA_{BET}) of *ca.* 621 $m^2\ g^{-1}$. Based on the Type-I shape of N_2 adsorption isotherm and assuming the absence of meso- and macro-pores, we also fit the isotherm with Langmuir method (Fig. S9, ESI†) and obtained the average

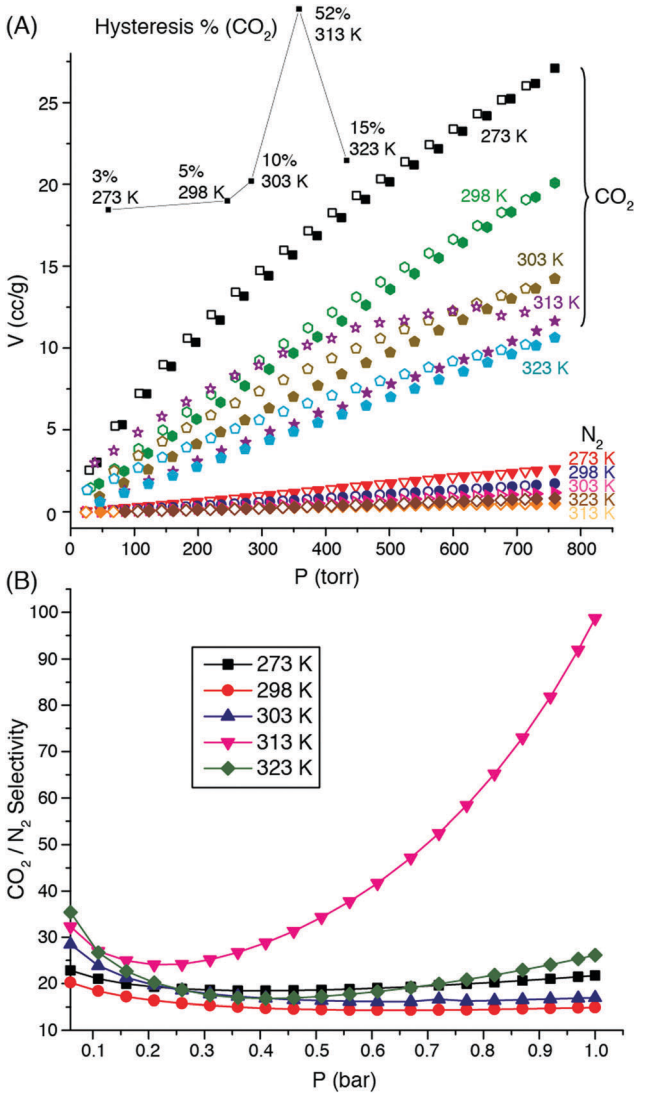

Fig. 2 (A) Adsorption/desorption isotherms of CO_2 and N_2 on **UNM-1** at various temperatures; inset: hysteresis percentages of CO_2 adsorption/desorption isotherms; (B) ideal CO_2/N_2 selectivities at different temperatures and pressures.

$SA_{Langmuir}$ of *ca.* 915 $m^2\ g^{-1}$. Thus, the surface area of **UNM-1** is among the highest in MOFs with four-fold interpenetrated structures,[27,28] which is likely resulted from the rigid borate arms and absence of charge compensating free ions. The pore-size distribution was estimated by fitting the N_2 adsorption isotherm at 77 K using non-local density functional theory (NLDFT) as shown in Fig. S10 (ESI†). A monomodal size-distribution with pore-diameter of *ca.* 6.14 Å was obtained, which is consistent with the microporous structure revealed by single crystal X-ray analysis.

The N_2 and CO_2 adsorption isotherms of **UNM-1** at 273 K, 298 K, 303 K, 313 K and 323 K are shown in Fig. 2A. These temperatures are relevant in real-world applications including CO_2 capture from industrial flue gases.[29,30] It is clearly seen that the adsorption of CO_2 by **UNM-1** is much enhanced over that of N_2 at all temperatures tested, up to *ca.* 27 cc per g CO_2 at

273 K and 1 bar (the pressure limit of the available instrument). It is noted that, although the amount of CO_2 adsorbed decreases with increasing temperature, the adsorption/desorption isotherms display increasing hysteresis that reaches a maximum of 52% at 313 K (Fig. 2A, inset).[31] The selectivity between CO_2 and N_2 is then calculated based on the ideal adsorbed solution theory (IAST)[32,33] by using the pyIAST code developed by Simon *et al.*,[34] assuming a flue gas like mixture containing 15% CO_2 and 85% N_2.[35–37] Detailed isotherm fitting parameters and ideal selectivity at various pressures and temperatures are given in the ESI,† and summarized in Fig. 2B. The ideal CO_2/N_2 selectivities are above 10 for all temperatures and pressures considered, and are relatively constant throughout the pressure range of 0–1 bar at 273 K, 298 K, 303 K and 323 K. Intriguingly, the ideal selectivity at 313 K displays an increase with increasing pressure and reaches *ca.* 99 at 1 bar, suggesting potentially effective CO_2 capture at flue gas conditions. In addition, the isosteric heat of CO_2 adsorption (Q_{ST}) on **UNM-1** is estimated to be between 27 ± 2 kJ mol^{-1} at 0.15 mmol g^{-1} CO_2 adsorption and 21 ± 4 kJ mol^{-1} at 0.5 mmol g^{-1} CO_2 adsorption using Clausius–Clayperon equation, and *ca.* 16 kJ mol^{-1} at 0 mmol g^{-1} CO_2 adsorption by Virial fitting, respectively (ESI†).[38,39] It is thus interesting to see that the large selectivity observed at 313 K coincides with the largest adsorption/desorption hysteresis at the same temperature, even though the Q_{ST} values for CO_2 are relatively small. We are currently studying this phenomenon in more detail by using in-situ IR spectroscopy to uncover the gas/solid interactions at the molecular level.

In summary, we have designed and synthesized a new charge separated MOF free of counter-ions, possessing high environmental stability and relatively large surface area, while showing promising characteristics for CO_2 separation. We are currently investigating the adsorption behaviors of **UNM-1** with other industrially important gases including H_2 and CH_4, and modifying the lengths and chemistry of the four arms of borate center, which can lead to a variety of charge-separated MOFs with tailor-designed structures and properties.

Y. Q. would like to acknowledge National Science Foundation (DMR-1453083) and United States Department of Agriculture (NIFA 2015-38422-24059) for financial support for this research.

Conflicts of interest

There are no conflicts to declare.

Notes and references

1 S. Kaskel, *The Chemistry of Metal-Organic Frameworks. Synthesis, Characterization, and Applications*, Wiley-VCH Verlag GmbH & Co., Weinheim, Germany, 2016.
2 S. M. Cohen, *Chem. Rev.*, 2012, **112**, 970–1000.
3 H. Furukawa, K. E. Cordova, M. O'Keeffe and O. M. Yaghi, *Science*, 2013, **341**, 1230444.
4 T. R. Cook and P. J. Stang, *Chem. Rev.*, 2015, **115**, 7001–7045.
5 J. A. Johnson, X. Zhang, X. Zhang and J. Zhang, *Curr. Org. Chem.*, 2014, **18**, 1973–2001.
6 A. Karmakar, A. V. Desai and S. K. Ghosh, *Coord. Chem. Rev.*, 2016, **307**, 313–341.
7 T. Düren, Y.-S. Bae and R. Q. Snurr, *Chem. Soc. Rev.*, 2009, **38**, 1237–1247.
8 A. Mavrandonakis, E. Klontzas, E. Tylianakis and G. E. Froudakis, *J. Am. Chem. Soc.*, 2009, **131**, 13410–13414.
9 M. Higuchi, K. Nakamura, S. Horike, Y. Hijikata, N. Yanai, T. Fukushima, J. Kim, K. Kato, M. Takata, D. Watanabe, S. Oshima and S. Kitagawa, *Angew. Chem., Int. Ed.*, 2012, **51**, 8369–8372.
10 M. Pan, B.-B. Du, Y.-X. Zhu, M.-Q. Yue, Z.-W. Wei and C.-Y. Su, *Chem. – Eur. J.*, 2016, **22**, 2440–2451.
11 D. Aulakh, A. P. Nicoletta, J. B. Pyser, J. R. Varghese and M. Wriedt, *Dalton Trans.*, 2017, **46**, 6853–6869.
12 J. Zhang, M. Zhao, W. Xie, J. Jin, F. Xie, X. Song, S. Zhang, J. Wu and Y. Tian, *New J. Chem.*, 2017, **41**, 9152–9158.
13 T. A. Grigolo, S. D. de Campos, F. Manarin, G. V. Botteselle, P. Brandão, A. A. Amaral and E. A. de Campos, *Dalton Trans.*, 2017, **46**, 15698–15703.
14 L. Qin, Z.-Y. Sun, K. Cheng, S.-W. Liu, J.-X. Pang, L.-M. Xia, W.-H. Chen, Z. Cheng and J.-X. Chen, *ACS Appl. Mater. Interfaces*, 2017, **9**, 41378–41386.
15 C. Zhang, Y. Liu, L. Sun, H. Shi, C. Shi, Z. Liang and J. Li, *Chem. – Eur. J.*, 2018, **24**, 2718–2724.
16 S. Wang, Q. Yang, J. Zhang, X. Zhang, C. Zhao, L. Jiang and C.-Y. Su, *Inorg. Chem.*, 2013, **52**, 4198–4204.
17 M. B. Lalonde, R. B. Getman, J. Y. Lee, J. M. Roberts, A. A. Sarjeant, K. A. Scheidt, P. A. Georgiev, J. P. Embs, J. Eckert, O. K. Farha, R. Q. Snurr and J. T. Hupp, *CrystEngComm*, 2013, **15**, 9408–9414.
18 J. A. Johnson, B. M. Petersen, A. Kormos and E. Echeverría, *J. Am. Chem. Soc.*, 2016, **138**, 10293–10298.
19 B. H. Hamilton, K. A. Kelly, T. A. Wagler, M. P. Espe and C. J. Ziegler, *Inorg. Chem.*, 2002, **41**, 4984–4986.
20 B. H. Hamilton, K. A. Kelly, T. A. Wagler, M. P. Espe and C. J. Ziegler, *Inorg. Chem.*, 2004, **43**, 50–56.
21 B. H. Hamilton, T. A. Wagler, M. P. Espe and C. J. Ziegler, *Inorg. Chem.*, 2005, **44**, 4891–4893.
22 B. H. Hamilton, T. B. Cardon, G. A. Lorigan and C. J. Ziegler, *Dalton Trans.*, 2005, 2941–2944.
23 B. H. Hamilton and C. J. Ziegler, *Inorg. Chem.*, 2004, **43**, 4272–4277.
24 B. H. Hamilton, K. A. Kelly, W. Malasi and C. J. Ziegler, *Inorg. Chem.*, 2003, **42**, 3067–3073.
25 D. Türp, M. Wagner, V. Enkelmann and K. Müllen, *Angew. Chem., Int. Ed.*, 2011, **50**, 4962–4965.
26 S. Fischer, J. Schmidt, P. Strauch and A. Thomas, *Angew. Chem., Int. Ed.*, 2013, **52**, 12174–12178.
27 A. Burgun, R. S. Crees, M. L. Cole, C. J. Doonan and C. J. Sumby, *Chem. Commun.*, 2014, **50**, 11760–11763.
28 Y.-J. Xiao, C.-Y. Sun, G.-C. Yang, L. Zhao and Z.-M. Su, *Inorg. Chem. Commun.*, 2014, **46**, 248–250.
29 D. Aaron and C. Tsouris, *Sep. Sci. Technol.*, 2005, **40**, 321–348.
30 M. Radosz, X. Hu, K. Krutkramelis and Y. Shen, *Ind. Eng. Chem. Res.*, 2008, **47**, 3783–3794.
31 The hysteresis at a given temperature is calculated as the ratio of the difference of the amount of adsorbed CO_2 between adsorption and desorption at 0.5 bar over the difference of the amount of adsorbed CO_2 between 0 and 1 bar at that temperature.
32 A. L. Myers and J. M. Prausnitz, *AlChE J.*, 1965, **11**, 121–127.
33 E. Richter, W. Schutz and A. L. Myers, *Chem. Eng. Sci.*, 1989, **44**, 1609–1616.
34 C. M. Simon, B. Smit and M. Haranczyk, *Comput. Phys. Commun.*, 2016, **200**, 364–380.
35 J. A. Mason, K. Sumida, Z. R. Herm, R. Krishna and J. R. Long, *Energy Environ. Sci.*, 2011, **4**, 3030–3040.
36 W. Lu, W. M. Verdegaal, J. Yu, P. B. Balbuena, H.-K. Jeong and H.-C. Zhou, *Energy Environ. Sci.*, 2013, **6**, 3559–3564.
37 X. Zhang, W. Chen, W. Shi and P. Cheng, *J. Mater. Chem. A*, 2016, **4**, 16198–16204.
38 X. Lv, L. Li, S. Tang, C. Wang and X. Zhao, *Chem. Commun.*, 2014, **50**, 6886–6889.
39 R.-J. Li, M. Li, X.-P. Zhou, D. Li and M. A. O'Keeffe, *Chem. Commun.*, 2014, **50**, 4047–4049.